HSM2025-44985

MULTI-SENSOR MONITORING OF WHEEL WEAR DURING CBN GRINDING OF CRANKSHAFT STEEL

C. Salame[1]*, P. Hoier[1], P. Krajnik[1], A. Malakizadi[1]

[1]Department of Industrial and Materials Science, Chalmers University of Technology, SE-412 96, Gothenburg, Sweden

*Corresponding author; e-mail: salamec@chalmers.se

Abstract
Monitoring grinding wheel wear is crucial for optimising dressing intervals and workpiece surface integrity. Grindability tests were conducted on a through-hardened, micro-alloyed C38 steel, using a multi-sensor approach to analyse forces and acoustic emission (AE) under varying grinding aggressiveness and wheel micro-topographies. The acquired data enabled the identification of features sensitive to wheel wear progression. For all investigated conditions, a worn wheel (duller micro-topography) led to higher forces and instantaneous energies of the AE Intrinsic Mode Functions. The frequency spectra obtained by Fast Fourier and Hilbert-Huang transforms also revealed distinct differences as wheel wear progressed.
Keywords:
acoustic emission, wear monitoring, process optimisation, grinding

1 INTRODUCTION

Grinding is a finishing process typically employed for the manufacture of precision components, where high requirements for form accuracy, dimensional tolerance, and surface integrity must be met. Cubic Boron Nitride (cBN) grinding wheels are particularly valued for their superior hardness, thermal stability, and long service life compared to conventional abrasives. However, as cBN wheels wear over time, their performance deteriorates, leading to reduced machining robustness and increased grinding forces. Further, the surface condition of a grinding wheel significantly influences the quality of the ground workpiece, as the wheel topography changes due to wear mechanisms such as attritious wear, grit fracture, and bond fracture [Malkin 2008]. In industrial grinding operations, dressing intervals are typically preset – determined without direct feedback on the actual wear state of the wheel – leading to conservative dressing strategies aimed at preventing defects such as thermal damage, poor surface finish, and dimensional inaccuracies. As a result, grinding wheels are often dressed earlier than necessary, increasing wheel consumption and reducing process efficiency.

Effective monitoring of cBN wheel wear is therefore essential for optimising grinding performance and extending tool life. Direct wear evaluation methods, such as optical microscopy and scanning electron microscopy (SEM), can be employed to assess the grinding wheel topography and quantify wear. While these techniques offer high accuracy and reliability, they interfere with the process, requiring interruption of grinding and sometimes destruction of the costly grinding wheels.

In contrast, indirect monitoring techniques using different sensors enable real-time assessment of wheel surface conditions during grinding. These methods provide continuous, non-intrusive monitoring, making them more practical for industrial implementation [Wegener 2011], and support adaptive dressing strategies that improve both productivity and cost-effectiveness. Previous work in wheel wear monitoring has focused on the use of sensors such as accelerometers [Mahata 2021], dynamometers [Shu 2023], power measurement [Guo 2007], and acoustic emission (AE) sensors [Badger 2018].

Among various sensors, AE sensors have proven to be the most promising for detecting wheel wear. During grinding, AE signals primarily originate from mechanisms such as elastic impact, grit fracture, bond fracture, friction, and the formation of indentation cracks, making AE highly effective for monitoring grinding wheel wear [Karpuschewski 1999]. Researchers have developed AE-based feature extraction techniques – such as root mean square (RMS), signal energy, and various frequency domain strategies – to correlate AE signals with wear states [Tönshoff 1999]. Despite promising results, challenges in data processing and real-time implementation remain areas of active research.

Dynamometers, on the other hand, can indicate variations in grinding conditions due to wheel wear through the measurement of grinding forces. Increases in normal and tangential forces have been linked to attritious wear and bond fracture [Malkin 2008]. Despite their accuracy, dynamometers are often less desirable in industrial settings due to their high cost and the potential need for machine reconfiguration [Zhang 2024].

This research investigates the use of AE sensors and dynamometers for monitoring cBN grinding wheel wear. For this purpose, two sets of surface grinding tests were conducted to investigate the influence of wheel micro-topography on the resulting signal responses.

The first set of tests, referred to as the *grindability tests*, was designed to evaluate variations in grinding forces and AE signals under different grinding conditions and wheel micro-topographies, i.e., wheel sharpness. Prior to each test, the grinding wheel was dressed dull, medium, or sharp – to generate different levels of wheel sharpness corresponding to various stages of wheel wear. The acquired force and AE signals were processed in the time domain, while the AE signals were further analysed using signal processing techniques, including Fast Fourier Transform (FFT) and Hilbert-Huang Transform (HHT), to extract potential features sensitive to the wheel sharpness/wear.

To further evaluate the sensitivity and robustness of the extracted features to progressive wheel wear, a longer grinding test was conducted without intermediate dressing – referred to as the *no-dress test*. This test aimed to monitor the evolution of the wheel's micro-topography and its influence on the force and AE features over time. This study thus evaluates the potential of various signal-processing methods in the context of wheel wear monitoring, offering more accessible and cost-effective solutions for industrial grinding applications.

2 THEORETICAL FOUNDATION OF SIGNAL PROCESSING

Signal processing in both time and frequency domain offer complementary approaches for analysing and interpreting signals. Time-domain (TD) methods require minimal processing and are computationally efficient, making them efficient for real-time applications. Features such as the root mean square (RMS) of the signal can provide valuable insights into the progression of a signal. However, TD methods may not capture the detailed frequency characteristics embedded within a signal [Shen 2022].

Frequency domain (FD) methods, on the other hand, offer insight into the spectral composition of signals, enabling the identification of frequency-dependent features that may be obscured in the time domain. However, this often comes at the cost of increased computational complexity and the need for transformations that may obscure temporal dynamics [Shen 2022]. Traditional FD methods, such as the Fast Fourier transform (FFT), decompose time-based signals into their constituent frequency components. However, FFT-based approaches assume signal stationarity and inherently lose time-localisation information, which limits their effectiveness in analysing non-stationary or transient signals where both time and frequency resolution are essential, as is the case in grinding operations [Huang 2008]. Despite their limitations, FFT can offer useful insight into the frequency composition of a signal. Further, the spectral centroid S_c represents the center of gravity of a spectrum and provides an indication of its average frequency content, while the spectral variance S_v quantifies the extent to which the signal's energy is dispersed across its frequency range. The spectral centroid can be calculated as,

$$S_c = \frac{\sum_i E_i \cdot f_i}{\sum_i E_i} \tag{1}$$

where f_i is the instantaneous frequency at point i and E_i is the amplitude at frequency f_i. The spectral variance is then calculated as,

$$S_v = \frac{\sum_i E_i \cdot (f_i - S_c)^2}{\sum_i E_i} \tag{2}$$

In contrast to FD methods, time-frequency (TFD) methods such as Hilbert-Huang transforms address several inherent limitations of FD approaches like the Fast Fourier Transform (FFT). These methods enable simultaneous representation of both time and frequency information by projecting one-dimensional time-series signals onto a two-dimensional time-frequency plane [Huang 2008]. The HHT is executed through a two-stage process: initially, Empirical Mode Decomposition (EMD) is applied to decompose the input signal into a finite set of intrinsic mode functions (IMFs). Subsequently, Hilbert Spectral Analysis is performed on the IMFs to extract their instantaneous frequency and energy distributions [Huang 2008].

The EMD decomposition reveals the signal's IMFs, which are the different oscillatory modes that compose the original signal. The obtained signal then undergoes an iterative sifting process to eliminate background waves and increase the symmetry of the wave profiles. A successfully extracted IMF is characterised by two conditions: it must exhibit an equal number of zero-crossings and extrema, and its upper and lower envelopes – formed by the local maxima and minima – must be symmetric [Huang 2008]. After decomposing a signal into its intrinsic mode functions (IMFs), the Hilbert transform is applied individually to each IMF. The Hilbert transform of a signal $x(t)$ is mathematically expressed as:

$$y(t) = \frac{p}{\pi} \int_{-\infty}^{\infty} \frac{x(\tau)}{t - \tau} d\tau \tag{3}$$

In Eq. 3, p represents the Cauchy principal value of the HHT. The Hilbert transform performs a convolution of a signal with $1/t$. From this, the analytic signal $z(t)$ can be constructed by coupling the signal $x(t)$ with its Hilbert transform $y(t)$ as follows,

$$z(t) = x(t) + iy(t) = a(t)e^{i\varphi(t)} \tag{4}$$

$$\text{where } a(t) = \sqrt{(x^2(t) + y^2(t))} \tag{5}$$

$$\text{and } \varphi(t) = \tan^{-1} \frac{y(t)}{x(t)}. \tag{6}$$

Here, $a(t)$ and $\varphi(t)$ denote the instantaneous amplitude and phase of the analytic signal $z(t)$, respectively. The instantaneous frequency $w(t)$ can then be derived from,

$$w(t) = \frac{d\varphi(t)}{dt} \tag{7}$$

3 EXPERIMENTAL SETUP AND MEASUREMENT SYSTEM

3.1 Experimental procedures

The workpiece material was a medium-carbon micro-alloyed steel used for heavy-duty automotive crankshafts. Cuboidal workpieces of 100x14x18 mm^3 were extracted from the half radius region of a hot-rolled steel bar. The workpieces were through hardened at 870 °C austenitisation temperature for 1 hour followed by water quenching. The workpieces were then tempered at 185 °C for 1 hour, resulting in an average hardness of 635 HV5.

The grinding tests were conducted on a Blohm Planomat HP 408 surface grinding machine using a synthetic grinding fluid (Quakercool 2920 EVC) at an 8% concentration. The setup is shown in Fig. 1. B181 VSS 1127G8SN V380 E vitrified cBN grinding wheel was used, with a diameter of 400 mm and a width of 20 mm. The dressing utilised a rotating diamond disc mounted on a rotary dressing unit.
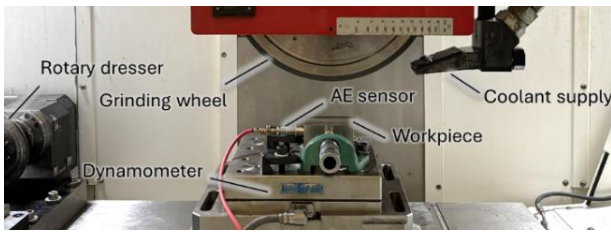
Fig. 1: Experimental setup of surface grinding tests.

A summary of the grinding and dressing parameters is provided in Tab. 1. The wheel and table speeds were kept constant, while the depth of cut was varied between 0.001 and 0.007 mm. This resulted in three different grinding aggressiveness numbers (*Aggr* = 13.5, 27.1 and 35.8), a widely adopted dimensionless parameter computed as described in [Badger 2021]. For the grindability tests, the wheel micro-topography was controlled via dressing prior to each test by varying the disc traverse speed. The employed traverse speeds gave three different overlap ratios (i.e., 3.5, 7.0, 10.5), corresponding to sharp, medium, and dull wheel micro-topographies, respectively. This resulted in a total of nine test conditions: three wheel states across three grinding conditions. For each of these conditions, a number of surface grinding passes were conducted, during which grinding forces and AE signals were acquired and analysed, as discussed in section 3.2.

Tab. 1: Grinding and dressing parameters during surface grinding experiments.

Grinding parameters		
Wheel speed	[m/s]	70
Table speed	[mm/min]	36000
Depth of cut	[mm]	0.001, 0.004, 0.007
Grinding width	[mm]	18 (grindability tests), 7 (no-dress test)
Dressing parameters		
Wheel speed	[m/s]	70
Dressing depth	[mm]	0.002
Speed ratio	[-]	+0.8
Traverse speed	[mm/s]	48.0, 24.0, 10.9
Overlap ratio	[-]	3.5, 7.0, 10.5

For the no-dress test, one grinding condition was selected due to the high volume of workpiece material removed required. The wheel speed was set at 70 m/s with a depth of cut of 0.007 mm, table speed of 36000 mm/min, and grinding width of 7 mm. The grinding wheel was initially dressed to a sharp condition (with an overlap ratio of 3.5), after which grinding of the workpiece was conducted in successive passes without dressing the wheel in order to allow the wear of the wheel to occur. This no-dress test was completed after 3900 passes, where the material removed per mm of wheel width (MR) reached 2,730 mm³/mm. The force and AE signals were also acquired as discussed in section 3.2.

3.2 Sensors and signal acquisition

To monitor tangential and normal forces during the grinding process, workpieces were mounted on a dynamometer (Kistler, type 9255C) which was fixed to the machine's table. For AE monitoring, the Accretech's (SB-3276) sensor was attached to the work-holding vice. Both signals were acquired by a National Instruments data acquisition (DAQ) system (cDAQ chassis NI-9174 with NI-9215 voltage input module) sampling the force and AE signals at 3 kHz and 100 kHz respectively.

For each grinding pass, the DAQ collected 3 signals: normal force (F_n), tangential force (F_t) and acoustic emission (*AE*). No signal shifting was required since the data collected by the DAQ was already synced to the same time scale. Signal segmentation of each signal allowed the extraction of the segments pertinent to active grinding, whereby the segments where the wheel was not engaged with the workpiece were excluded. The investigated frequency range of the AE signal was set to 0-50 kHz to satisfy the Nyquist criteria with a 100 kHz acquisition rate.

During the grindability tests, the force and AE signals were acquired and analysed from 5 repetitions (5 passes) for each of the 9 test conditions.

For the no-dress test, the forces were measured and analysed at various intervals, more frequently towards the beginning of the test to monitor the break-in of the wheel. The AE signals were analysed from 5 distinct segments (S1-S5) captured at various stages of the no-dress test. Each segment corresponds to 3.0 seconds of active grinding, equivalent to a workpiece material removed of 12.60 mm³/mm. To ensure measurements were taken in stable grinding condition (after wheel break-in as identified by the force stabilisation), the initial segment analysed (S1) begins after an accumulated MR of 70 mm³/mm. Subsequent segments S2 through S5 were collected following MRs of 669.9, 1352.4, 2034.9, and 2717.4 mm³/mm, respectively.

3.3 Signal post-processing and feature extraction

The analysis of the grinding forces F_n and F_t in this work primarily focused on their mean values and determining the specific energy associated with the grinding process.

The acoustic emission signals, on the other hand, were subject to various time, frequency and time-frequency post-processing. The TD features, extracted from the raw signal, included the root mean square, variance, skewness and kurtosis. For the FD analysis, the FFT transform was applied, and the mean FFT amplitude was computed across 20 equally spaced frequency bins. In addition, the spectral centroid and spectral variance were calculated to differentiate between various wheel conditions. As for the TFD analysis, the HHT transform was applied, and the instantaneous energy was extracted for the first 4 IMFs. For each IMF, the mean instantaneous energy was computed across 20 equally spaced frequency bins, and the spectral centroid and variance were calculated. The extracted features from the AE signals are summarised in Tab. 2.

Tab. 2: Tested extracted features using the AE signals and their extraction source.

Domain	Source	Extracted features
TD	Raw signal	- RMS, variance, skewness, kurtosis
FD	FFT Amplitudes	- Spectral centroid - Spectral variance - Frequency bin amplitudes
TFD	HHT-IMFs	- Spectral centroid - Spectral variance - Mean instantaneous energy - Frequency bin energies

4 RESULTS AND DISCUSSION

4.1 Grindability tests

The results presented in this section refer to the grindability tests conducted using different aggressiveness (*Aggr* = 13.5, 27.1 and 35.8) and wheel conditions (sharp, medium

and dull). Fig. 2(a) presents the variation in normal (F_n) and tangential forces (F_t) for each of the investigated conditions, where an increase in aggressiveness leads to the expected increase in both normal and tangential forces. The wheel with the duller micro-topography also exhibits significantly higher forces for identical grinding conditions. For instance, at the highest aggressiveness, the normal force is 82% and 154% higher for a medium and dull wheels, respectively, compared to the sharp one. A similar trend is observed for the tangential force, with increase of 72% and 156% for a medium and dull wheels, respectively, compared to the sharp wheel.
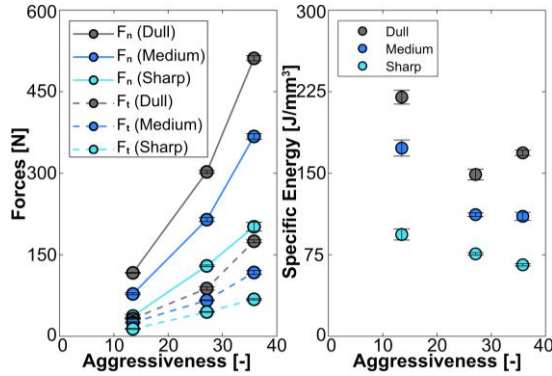
Fig. 2: (a) Normal and tangential forces and (b) specific energy for different aggressiveness and wheel conditions

Fig. 2(b) shows the obtained specific energy curves. As expected, the specific energy is notably higher for a duller wheel under the same grinding conditions. At the intermediate aggressiveness, for instance, the specific energy increases by 48% and 96%, respectively, when grinding with a medium or dull wheel compared to a sharp one – making chip formation less efficient.

Regarding the analysis of the acoustic emission signals from a time domain perspective, the extracted features are summarised in Tab. 3 for the lowest and highest aggressiveness tests. As evident, the RMS and variance both exhibit a progressive increase from sharp to medium to dull wheel, while the skewness and kurtosis follow the opposite trend. This implies that as the wheel becomes duller, the signal undergoes more significant fluctuations and greater energy, while the distribution of the signal becomes more symmetric and less peaked. In fact, these trends hold for *Aggr* = 27.1 as well.

Tab. 3: Time-domain extracted features of AE signals

	Aggr = 13.5			*Aggr* = 35.8		
	Sharp	Med.	Dull	Sharp	Med.	Dull
RMS [-]	0.10	0.11	0.32	0.36	0.64	0.93
Variance [-]	0.01	0.01	0.09	0.11	0.39	0.85
Kurtosis [-]	5.92	3.38	1.76	1.84	0.69	0.29
Skewness [-]	66.16	21.56	7.35	7.45	3.41	2.45

The frequency domain analysis of the AE signals using FFT for the case of *Aggr* = 35.8 shows the discrete frequency spectrum, presented in Fig. 3. The Fourier amplitudes, which reflect the contribution of a specific frequency within a signal, are averaged and classified into 20 equally spaced frequency bins. As evident, there is a clear distinction in the FFT amplitudes, where the medium and dull wheel show a notable increase compared to a sharp wheel across all frequency bins. In fact, the same trends are observed for the other investigated grinding conditions, with all frequency bins successfully identifying different wheel wear states.
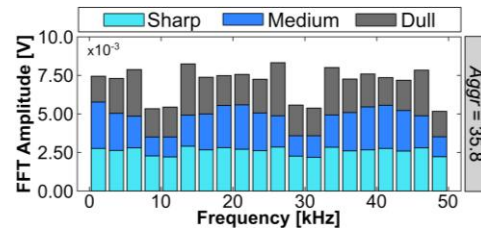

Fig. 3: Discrete frequency spectrum comparing the mean AE FFT amplitudes for a sharp, medium and dull wheel

Further analysis of the FFT provided the spectral centroid and variance plots shown in Fig. 4(a). The spectral centroid shifts towards higher frequencies as the wheel becomes duller. Additionally, lower aggressiveness levels appear to exhibit higher spectral centroids compared to more aggressive grinding conditions. This suggests that both wheel dullness and less aggressive grinding are associated with increased prominence of higher frequency components in the acoustic emission spectrum.

Fig. 4(b) shows that the spectral variance decreases with both increasing wheel dullness and increasing grinding aggressiveness. This indicates that the frequency content of the acoustic emission signals becomes more concentrated around the spectral centroid, suggesting a reduction in the diversity of frequency components as the wheel wears and the grinding becomes more aggressive.
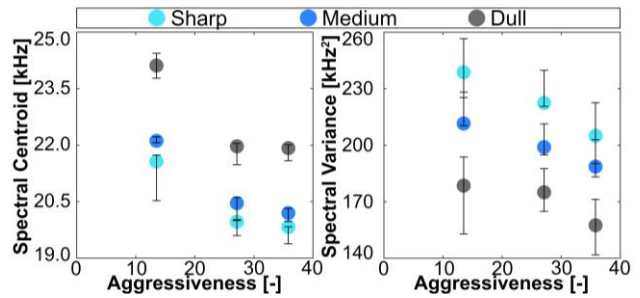

Fig. 4: (a) FFT spectral centroid and (b) spectral variance variations for AE signals of different grinding conditions
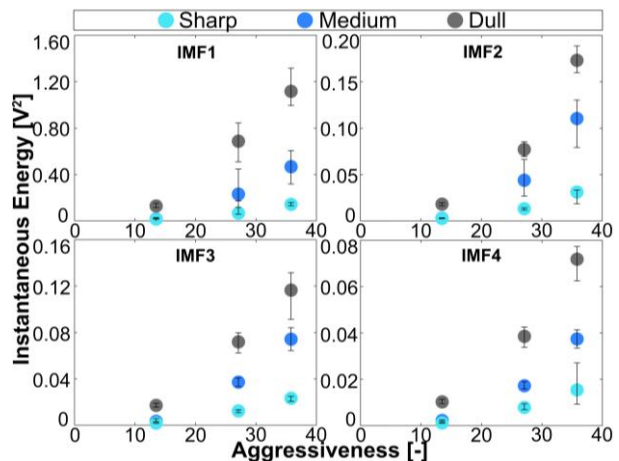

Fig. 5: Mean instantaneous energy of the different IMFs for different wheel and grinding conditions

In the TFD analysis, the Hilbert-Huang Transform (HHT) was applied to the Intrinsic Mode Functions (IMFs) extracted from the AE signals. As shown in Fig. 5, the mean instantaneous energy effectively reflects the micro-topography of the grinding wheel. All four IMFs, across the three tested grinding conditions, follow the same trend: the mean instantaneous energy increases progressively from the sharp to the medium and to the dull wheel. This trend likely reflects the effects of wheel wear,

which leads to larger portions of ploughing and sliding during the grinding process – all of which are significant contributors to acoustic emission.

4.2 No-dress test

The no-dress test was performed to evaluate the robustness of the investigated extracted features when the wheel is not dressed between subsequent grinding passes. Under such conditions, the features should be particularly sensitive to changes in wheel micro-topography due to wear.

The test was run for a total volume of material removed of 2730 mm³/mm, after which the wheel was inspected for wear. Since only part of the wheel width – corresponding to the grinding width of 7 mm – was engaged during the process, a "razor blade" test could be performed to measure wear. Here, wear is induced on a localized section of the wheel surface, creating a step relative to the unused portion. The measurement revealed microscopic edge wear, with the depth of edge wear (Δr_{sk}) increasing from an initial 35 µm to 118 µm. No notable step was observed at the transition zone of the wheel, indicating no macroscopic wheel wear. Fig. 6 shows the normal and tangential force measurements throughout the test, where the force experiences a sharp decrease in the initial phase, identified as the wheel break-in [Malkin 2008]. The normal force then exhibits a slight but gradual increase from 77.2 N to 87.1 N (12.8% increase). The tangential force does not experience a similar increase and is rather stable at 29 N, attributed to insignificant wear. Fig. 6 also shows the approximate regions from which the 5 segments S1-S5 were extracted for the AE signal analysis.
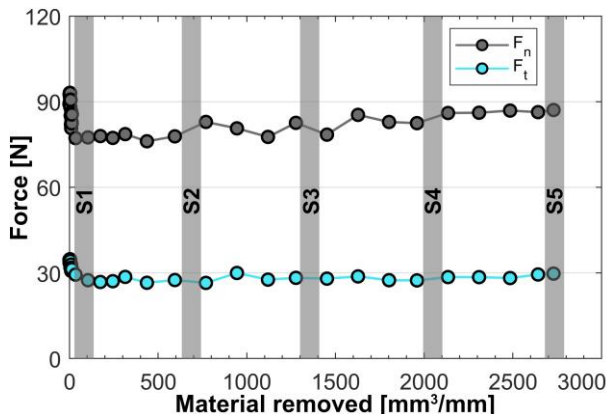

Fig. 6: Normal and tangential force progression with respect to material removed (width of S1-S5 not to scale)

When analysing the raw AE signals in the time domain, the RMS, variance, kurtosis, and skewness were extracted. While kurtosis and skewness showed no discernible trend, both RMS and variance exhibited steady increases from S1 to S5. Specifically, the RMS increased from 0.19 to 0.29 (52%) and the variance rose from 0.044 to 0.095 (116%). These trends suggest that as wear progresses, the signal undergoes greater fluctuations and an increase in energy.

From a FD perspective, the discrete frequency spectra of each segment, obtained using the FFT and presented in Fig. 7, do not exhibit any clear trends – unlike their behaviour in the grindability tests. This discrepancy may be attributed to the relatively minimal wear in the no-dress test, as opposed to the significantly different micro-topographies induced in the grindability experiments. Additionally, the limitations of the FFT in handling non-stationary and non-linear signals likely contribute to its insensitivity to subtle wear changes. These findings suggest that FFT-based spectral analysis may be insufficient for early wear

detection in industrial settings, where timely identification of even minimal wheel wear is critical – well before reaching the dull wheel condition identified in the grindability tests.
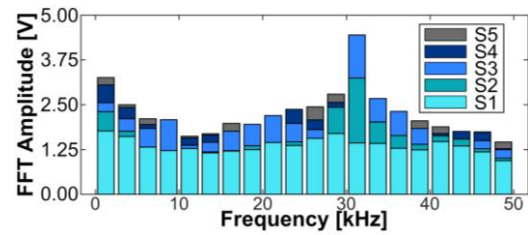

Fig. 7: Discrete AE-frequency spectrum of the mean FFT amplitudes for segments S1-S5

In contrast to the limitations of the FFT, the HHT approach demonstrates consistent trends with those observed in the grindability tests. Specifically, the mean instantaneous energy increases progressively with wear, as illustrated in Fig. 8. Although there is some overlap between the error bars, this is likely due to the comparatively lower wear progression between consecutive segments in the no-dress test. This trend is consistent across all four IMFs: IMF1 shows an increase of 272% from S1 to S5, while IMF2, IMF3, and IMF4 exhibit increases of 111%, 129%, and 250%, respectively.
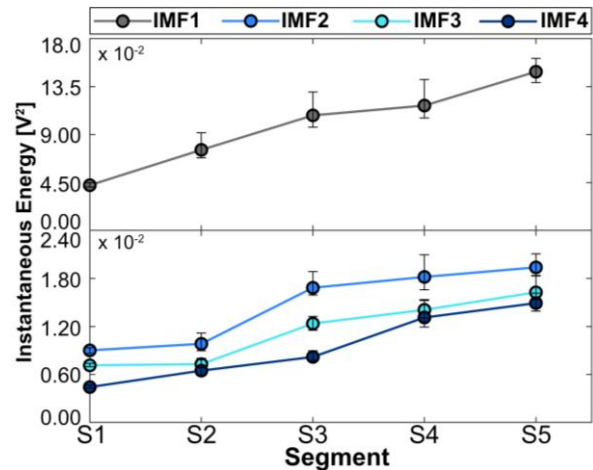

Fig. 8: Progression of HHT mean instantaneous energies for IMFs 1-4 for segments S1-S5

A more detailed spectral analysis of the IMFs across specific frequency bands reveals a notable trend, as observed in Fig. 9. The mean HHT energy in certain frequency bins shows a progressive increase with wear, increasingly gradually for each subsequent segment. The frequency bins in which this trend occurs vary by IMF, indicating that each IMF captures energy changes in distinct frequency regions. For IMF1, a clear distinction across all five stages is observed in approximately 50% of the frequency bins, particularly in the higher-frequency range. As the analysis moves to IMF2, IMF3, and IMF4, the frequency bins exhibiting this trend shift toward lower frequencies, while the percentage of bins showing progressive increases remains relatively stable – around 45% for IMF2 and IMF3, and 50% for IMF4.

The further investigation of the spectral features of the IMFs reveals distinct trends in the spectral centroid of the 3rd and 4th IMFs, both of which shift towards higher frequencies as wear progresses, as shown in Fig. 10. The increase in spectral centroid from S1 to S5 is 4% and 26% for IMF3 and IMF4, respectively. Similarly, the spectral variance shows an increasing trend for IMF2 and IMF4 from segments S1 to S5 by 4% and 37%. This suggests that as the grinding

wheel wears, the frequency content of the IMF spectrum becomes less concentrated around the spectral centroid. Notably, this increase appears to plateau across segments S3, S4, and S5, indicating a slower rate of change in later stages of wear. These trends indicate that, as wheel wear progresses, the frequency content of the IMFs shifts to higher frequency components but becomes dispersed.
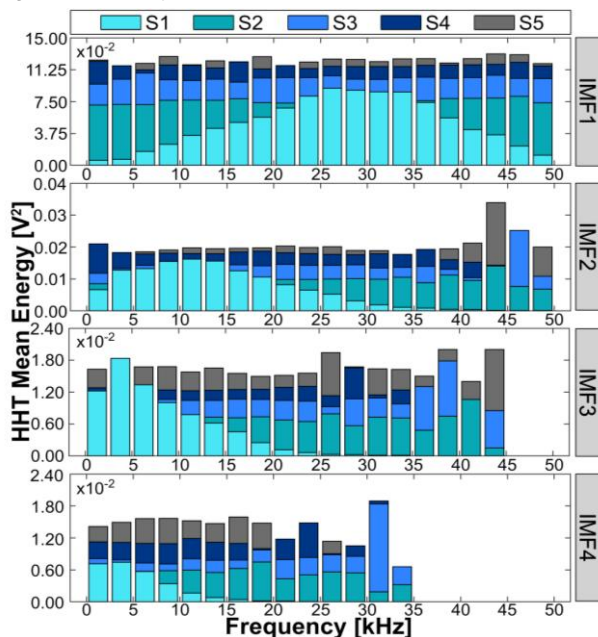

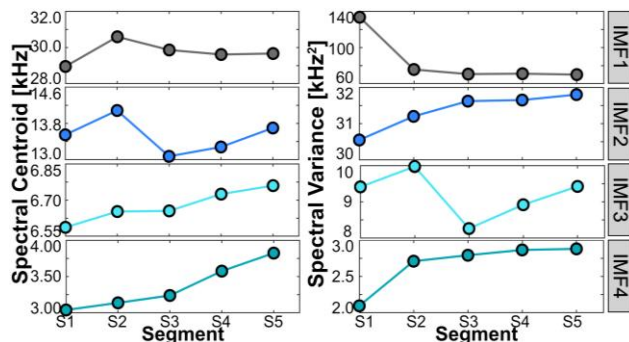*Fig. 9: Discrete AE-frequency spectrum of the mean HHT energy for IMFs 1-4 acquired from segments S1-S5*

Fig. 10: Comparison of spectral centroid and spectral variance for different IMFs for segments S1-S5

5 CONCLUSIONS

A multi-sensor monitoring approach was successfully employed to detect grinding wheel wear, revealing consistent correlations between sensor features and wheel condition. The main conclusions are as follows:

- The force measurements showed a clear increase in normal and tangential forces with increased wear.
- The time-domain analysis of the AE signal showed an increase in RMS and variance as wear progressed.
- Time-frequency analysis using HHT proved more effective than traditional FFT-based methods in detecting gradual wear progression, with the mean HHT instantaneous energy of AE signals showing a clear and repeatable increase across all IMFs.
- The spectral centroid and variance showed that the frequency content of the IMFs shifted towards higher frequencies and became more dispersed with wear.

- A spectral analysis of IMFs showed that the frequency ranges capturing wear-related changes varied by IMF, with higher-frequency bins in IMF1 and progressively lower-frequency bins in IMF2–IMF4.

These findings highlight the potential of various AE features as robust means for early detection of wheel wear, with implications for optimising dressing intervals and improving process robustness in industrial applications.

7 REFERENCES

[Badger 2018] Badger, J., et al. Acoustic Emission in Dressing of Grinding Wheels: AE Intensity, Dressing Energy, and Quantification of Dressing Sharpness and Increase in Diamond Wear-Flat Size. Int. Journal of Machine Tools and Manufacture, 2018, Vol. 125, pp.11-19.

[Badger 2021] Badger, J., et al. Application of the Dimensionless Aggressiveness Number in Abrasive Processes. Procedia CIRP, 2021, Vol. 102, pp. 361–368.

[Guo 2007] Guo, C., et al. Power and Wheel Wear for Grinding Nickel Alloy with Plated CBN Wheels. CIRP Annals, 2007, Vol. 56, No. 1, pp. 343–346.

[Huang 2008] Huang, N. E., and Wu, Z. A Review on Hilbert-Huang Transform: Method and Its Applications to Geophysical Studies. Reviews of Geophysics, 2008.

[Karpuschewski 1999] Karpuschewski, B., et al. Grinding Monitoring System Based on Power and Acoustic Emission Sensors. CIRP Annals, 1999, Vol. 48, No. 1, pp. 235–238.

[Mahata 2021] Mahata, S., et al. A Robust Condition Monitoring Methodology for Grinding Wheel Wear Identification Using Hilbert Huang Transform. Precision Engineering, 2021, Vol. 70, pp. 77–91.

[Malkin 2008] Malkin, S., and Guo, C. Grinding Technology: Theory and Application of Machining with Abrasives. Industrial Press Inc., New York, USA, 2008.

[Shen 2022] Shen, C.H. "Acoustic Emission Based Grinding Wheel Wear Monitoring: Signal Processing and Feature Extraction." Applied Acoustics, 2022, Vol. 196.

[Shu 2023] Shu, L., et al. Effect of Single-Grit Wear on Surface Integrity of Hardened Stainless Steel in Dry Grinding. CIRP Annals, 2023, Vol. 72, No. 1, pp. 259–262.

[Tönshoff 1999] Tönshoff, H.K., et al. Characterization of the Grinding Process by Acoustic Emission. International Journal of Machine Tools and Manufacture, 1999, Vol. 39, No. 4, pp. 593–598.

[Wegener 2011] Wegener, K., et al. Conditioning and Monitoring of Grinding Wheels. CIRP Annals, 2011, Vol. 60, No. 2, pp. 757–777.

[Yang 2014] Yang, Z., et al. Application of Hilbert–Huang Transform to Acoustic Emission Signal for Burn Feature Extraction in Surface Grinding Process. Measurement, 2014, Vol. 47, pp. 14–21.

[Zhang 2024] Zhang, Y., et al. Leveraging Artificial Intelligence for Real-Time Indirect Tool Condition Monitoring in Milling. International Journal of Machine Tools and Manufacture, 2024, Vol. 202.